



**Influence of surface functionalization on thermal transport  
and thermoelectric properties of MXene monolayers**

Journal:	<i>Nanoscale</i>
Manuscript ID	NR-ART-12-2017-009144.R2
Article Type:	Paper
Date Submitted by the Author:	19-Mar-2018
Complete List of Authors:	Sarı Kurt, Sevil; Dokuz Eylül Üniversitesi - Tinaztepe Kampusu Çakır, Deniz; University of North Dakota Keceli, Murat; Argonne National Laboratory Sevik, Cem; Anadolu University, Mechanical Engineering

# Influence of surface functionalization on thermal transport and thermoelectric properties of MXene monolayers

Sevil Sarikurt,<sup>1,\*</sup> Deniz Çakır,<sup>2,†</sup> Murat Keçeli,<sup>3,‡</sup> and Cem Sevik<sup>4,§</sup>

<sup>1</sup>*Department of Physics, Faculty of Science, Dokuz Eylül University, Izmir, 35390, TURKEY*

<sup>2</sup>*Department of Physics and Astrophysics, University of North Dakota, Grand Forks, North Dakota 58202, USA*

<sup>3</sup>*Chemical Sciences and Engineering Division, Argonne National Laboratory, Argonne, Illinois 60439, USA*

<sup>4</sup>*Department of Mechanical Engineering, Faculty of Engineering, Anadolu University, Eskisehir, 26555, TURKEY*

(Dated: April 6, 2018)

The newest members of two-dimensional material family, called transition metal carbides and nitrides (MXenes), have garnered increasing attention due to their tunable electronic and thermal properties depending on the chemical composition and functionalization. This flexibility can be exploited to fabricate efficient electrochemical energy storage (batteries) and energy conversion (thermoelectric) devices. In this study, we calculated the Seebeck coefficients and lattice thermal conductivity values of oxygen terminated  $M_2CO_2$  (where  $M=Ti, Zr, Hf, Sc$ ) monolayer MXene crystals in two different functionalization configurations (model-II (MD-II) and model-III (MD-III)), using Density Functional Theory and the Boltzmann Transport Theory. We estimated thermoelectric figure-of-merit,  $zT$ , of these materials by two different approaches, as well. First of all, we found that the structural model (i.e. adsorption site of oxygen atom on the surface of MXene) has a paramount impact on the electronic and thermoelectric properties of MXene crystals, that can be exploited to engineer the thermoelectric properties of these material. The lattice thermal conductivity  $\kappa_l$ , Seebeck coefficient and  $zT$  values may vary 40% depending on the structural model. The MD-III configuration always has the larger band gap, Seebeck coefficient and  $zT$ , and smaller  $\kappa_l$  as compared to the MD-II structure due to larger band gap, highly flat valence band and reduced crystal symmetry in the former. The MD-III configuration of  $Ti_2CO_2$  and  $Zr_2CO_2$  has the lowest  $\kappa_l$  as compared to the same configuration of  $Hf_2CO_2$  and  $Sc_2CO_2$ . Among all the considered structures, the MD-II configuration of  $Hf_2CO_2$  has the highest  $\kappa_l$ , and  $Ti_2CO_2$  and  $Zr_2CO_2$  in MD-III configuration have the lowest one. For instance, while the band gap of MD-II configuration of  $Ti_2CO_2$  is 0.26 eV, it becomes 0.69 eV in MD-III.  $zT_{max}$  value may reach up to 1.1 depending on the structural model of MXene.

## I. INTRODUCTION

The demonstration of peculiar electronic properties of graphene by Novoselov and co-workers<sup>1</sup> have led researchers to be intensively interested in other 2D materials such as hexagonal boron nitrides (h-BN), transition metal dichalcogenides (TMDs), metal oxides and more recently MXenes. MXenes are generally fabricated by chemically etching out of the A layers from MAX phases, which belong to a family of layered transition metal carbides and metal nitrides. The chemical formula of the MAX phase is given by  $M_{n+1}AX_n$  ( $n=1,2,3$ ), where M is an early transition metal, A is mainly an element from group IIIA or IVA and X is C and/or N.<sup>2</sup> After etching the A layer, the surface of each MXene layer has been terminated by surface groups such as F, H, OH and/or O due to the chemical fabrication process. The final functionalized MXene structures are given by the formula  $M_{n+1}X_nT_{n+1}$  ( $T= F, H, OH, O$ ).

Various experimental studies demonstrated that MXene crystals have extensive and growing application areas. Up to now,  $Ti_3C_2$ ,<sup>3</sup>  $Ti_2C$ ,  $Ta_4C_3$ ,  $TiNbC$ ,  $(V_{0.5}, Cr_{0.5})_3C_2$ ,  $Ti_3CN$ ,<sup>2</sup>  $Nb_2C$ ,  $V_2C$ ,<sup>4</sup>  $Nb_4C_3$ ,<sup>5</sup>  $Mo_2C$ ,<sup>6</sup>  $Mo_2TiC_3$ <sup>7</sup> and  $Ti_4N_3$ <sup>8</sup> layered MXene structures have been synthesized experimentally and some of these materials have been already proposed for different technological applications such as Li-ion batter-

ies,<sup>9–12</sup> super-capacitors,<sup>13–15</sup> fuel-cells,<sup>16</sup> hydrogen storage<sup>17,18</sup> and electronic devices.<sup>19,20</sup> Furthermore, experimental results on temperature dependent thermoelectric (TE) properties of freestanding MXene materials ( $Mo_2CT_x$ ,  $Mo_2TiC_2T_x$ ,  $Mo_2Ti_2C_3T_x$ ) have been reported recently.<sup>21</sup> The measurements showed that the Mo-based MXenes have high electrical conductivity and relatively large Seebeck coefficient values, that leads to a better TE performance for these materials than their parent ternary and quaternary layered carbides. Additionally, authors also proposed, based on their overall results, that this promising performance can further be enhanced by additional doping, controlling the surface functional groups, and/or hybridization with semiconductor materials or polymers.

Also, the electronic properties and the dynamical stability of some MXene structures have been investigated theoretically by different research groups. The thermoelectric properties of functionalized  $M_2C$  ( $M=Sc, Ti, V, Cr, Zr, Nb, Ta$ ) and  $M_2N$  ( $M=Ti, Cr, Zr$ ) structures with F, OH and O have been analyzed by Khazaei *et al.*<sup>22</sup> They considered four different functionalization models, Model I (MD-I) - Model IV (MD-IV), and obtained the most energetically stable ones. They have reported that  $Ti_2CO_2$ ,  $Hf_2CO_2$ ,  $Zr_2CO_2$ ,  $Sc_2CT_2$  ( $T=F, OH, O$ ) MXene structures exhibit semiconductor behaviour with a small band gap of 0.24, 1.0, 0.88, 1.03, 0.45 and 1.8 eV, respec-

tively. Their results suggested that  $\text{Ti}_2\text{CO}_2$  would be a good candidate for TE device applications. The structural, mechanical and electronic properties of  $\text{M}_2\text{CT}_2$  ( $\text{M}=\text{Sc, Ti, V, Cr, Zr, Nb, Mo, Hf, Ta, W}$ ) MXene structures have been investigated by Zha *et al.*<sup>23</sup> They have shown that transition metal atom and the surface functional groups ( $\text{T}=\text{F, OH, O}$ ) have considerable influence on the crystal structure of these materials and the oxygen functionalized MXene structures possessing smaller lattice parameters show superior mechanical stability as compared to fluorine and hydroxyl functionalized ones. In addition to the structural properties, the influence of the functionalization also on the electronic and thermal properties of MXene structures has been reported in several other studies.<sup>24–26</sup> Zha *et al.* have also investigated the electronic and thermal properties of  $\text{Sc}_2\text{CT}_2$  ( $\text{T}=\text{F, OH}$ ),<sup>27</sup> and  $\text{Hf}_2\text{CO}_2$ ,  $\text{Ti}_2\text{CO}_2$ , and  $\text{Zr}_2\text{CO}_2$ <sup>28</sup> MXene crystals. They have found that  $\text{Sc}_2\text{C(OH)}_2$  is the only semiconductor with intrinsic direct band gap among all the Sc based MXenes crystals that they have studied. Also, they have determined that the lattice thermal conductivity  $\kappa_l$  value increases with increasing atomic number of transition metals that they considered and showed that  $\text{Ti}_2\text{CO}_2$  might be a better candidate for nanoelectronic applications due its high electron mobility and also low  $\kappa_l$ . Furthermore, Gandi *et al.*<sup>29</sup> have performed calculations for the TE properties of  $\text{M}_2\text{CO}_2$  ( $\text{M}=\text{Ti, Zr, Hf}$ ) MXene structures and they have demonstrated that the band gap grows with increasing mass of the transition metal and  $\text{Ti}_2\text{CO}_2$  crystal has the best TE performance due to its lower  $\kappa_l$ . Yorulmaz *et al.*<sup>30</sup> have investigated the dynamical and mechanical stability of 80 functionalized  $\text{M}_2\text{XT}_2$  ( $\text{M}=\text{Sc, Mo, Ti, Zr, Hf}$ ;  $\text{X}=\text{C, N}$ ;  $\text{T}=\text{O, F}$ ) MXene structures systematically and reported the most energetically favorable models for each MXene system. They have found that MD-II and MD-III configurations of  $\text{M}_2\text{CO}_2$  ( $\text{M}=\text{Ti, Zr, Hf}$ ), MD-III configuration of  $\text{Sc}_2\text{CO}_2$  and  $\text{M}_2\text{CF}_2$  ( $\text{M}=\text{Sc, Zr, Hf}$ ) and also MD-II and MD-IV configurations of  $\text{Sc}_2\text{CF}_2$  MXene monolayers demonstrate semiconductor characteristics and stable dynamical properties. In summary, the recently reported experimental measurement and previous theoretical studies have clearly pointed out that the thermoelectric properties of MXene crystals are needed to be further examined, particularly taking into account surface effects.

Thermoelectric materials (TEMs) are mainly used for refrigeration and power generation through the conversion of a temperature gradient into electricity, or vice versa. Flexible in size and shape and without any mechanical parts, TE devices offer unique advantages compared to conventional refrigerators and generators. However, their usage is still limited due to their lower TE efficiency, which can be evaluated via dimensionless TE figure-of-merit defined as  $zT = S^2\sigma T/\kappa$ , where  $S$  is the Seebeck coefficient (or thermopower),  $\sigma$  is the electrical conductivity,  $T$  is temperature and  $\kappa$  is total thermal conductivity that includes contributions from the lattice

(phonon) thermal conductivity ( $\kappa_l$ ) and the electronic thermal conductivity ( $\kappa_e$ ). A good TE material should display a "high" power factor,  $S^2\sigma$  and "low" thermal conductivity,  $\kappa$ , but this elusive target has challenged researchers for decades. As mentioned above, the functionalized MXene materials have prominent electronic, mechanical and thermal properties<sup>22,27–30</sup> and thus it is imperative to study their electronic and thermal transport properties in order to estimate their potential as a thermoelectric material.

In this respect, we have calculated the electronic and thermal transport properties of  $\text{M}_2\text{CO}_2$  ( $\text{M}=\text{Ti, Zr, Hf, Sc}$ ) monolayer MXene crystals by utilizing first principles electronic structure calculations and solving linearized Boltzmann transport equation (BTE)<sup>31–33</sup> for both electrons and phonons. Our results provide qualitative and quantitative information on the importance of the chemical composition and structural configuration of different MXenes and guide experimental studies for materials with higher TE efficiency.

## II. COMPUTATIONAL METHOD

The electronic and thermal properties of all the considered systems were predicted by first-principles calculations based on density functional-theory (DFT) and density-functional perturbation theory (DFPT), as implemented in the Vienna Ab-initio Simulation package (VASP) code.<sup>34,35</sup> The exchange-correlation interactions were treated using the generalized gradient approximation (GGA) within the Perdew-Burke-Ernzerhof (PBE) formulation<sup>36</sup> and the single electron wave functions were expanded in plane waves with kinetic energy cutoff of 450 eV, for all the simulations. For the structure optimizations, the Brillouin-zone integrations were performed using a  $\Gamma$ -centered regular  $16\times 16\times 1$   $k$ -point mesh within the Monkhorst-Pack scheme.<sup>37</sup> The convergence criterion for electronic and ionic relaxations were set to  $10^{-7}$  eV and  $10^{-4}$  eV/Å, respectively. A 15 Å vacuum layer along the  $z$ -direction was adopted to prevent any interaction between neighboring layers.

Lattice thermal transport properties were determined by the self-consistent solution of Peierls-Boltzmann transport equation<sup>38</sup> as implemented in ShengBTE code.<sup>39</sup> Long-range electrostatic interactions (nonanalytic correction) are included by using the Born effective charges and dielectric tensor calculated by VASP. The second-order inter-atomic force constants (IFCs) required by the ShengBTE were obtained by PHONOPY<sup>40</sup> code which extracts the proper force-constant file from the results predicted by DFPT. The third-order IFCs were derived from the VASP calculations of the structures generated by considering up to seven (eight) next-nearest-neighbor interactions for MD-II (MD-III). Here,  $4\times 4\times 1$  supercell structures and a  $\Gamma$ -centered regular  $4\times 4\times 1$   $k$ -point mesh were used in the DFT calculations performed to predict the second- and third-order IFCs, respec-

tively. In lattice thermal transport calculations at least  $80 \times 80 \times 1$  well converged  $q$ -grid and  $6.00 \text{ \AA}$  out of plane lattice constant,  $d$ , were used for all the considered single layer materials to make a reliable comparison of monolayer structures with each other. The upper limit for the temperature range was set to  $700 \text{ K}$  to ensure that all MXene structures are solid, since molecular dynamics simulations predicted that  $\text{Ti}_2\text{CO}_2$  starts melting at  $823 \text{ K}$ .<sup>41</sup>

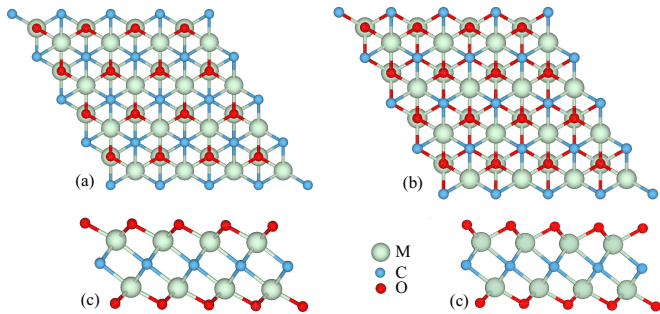


FIG. 1: (Color online) Schematic illustration of functionalized  $\text{M}_2\text{XT}_2$  MXene systems: Top views of (a) MD-II and (b) MD-III; side views of (c) MD-II and (d) MD-III.

Seebeck coefficient, the electrical conductivity ( $\sigma/\tau$ ) and the electronic thermal conductivity ( $\kappa_e/\tau$ ) were calculated by using relaxation time approximation as implemented in BoltzTraP<sup>42</sup> software package based on the Wiedemann-Franz law. Here, a  $\Gamma$ -centered regular  $64 \times 64 \times 1$   $k$ -point mesh were adopted to obtain the band energies to be used in BoltzTraP calculations. Although the relaxation time ( $\tau$ ) depends on the electronic wave vector, energy, and scattering mechanism, the relaxation time approximation (RTA) have been shown to provide reasonable results for various materials.

### III. RESULTS AND DISCUSSIONS

In this study, we systematically investigated and compare the thermoelectric potential of seven different semiconductor monolayer MXene structures,  $\text{M}_2\text{CO}_2$  ( $\text{M}=\text{Ti}, \text{Zr}, \text{Hf}, \text{Sc}$ ). Depending on the lattice positions of functional groups (here it is oxygen), we considered two different crystal configuration (MD-II & MD-III), depicted in Fig. 1, for all the monolayers except  $\text{Sc}_2\text{CO}_2$ , for which only semiconductor structure MD-III was considered.

The crystal symmetries of the MD-II and MD-III structures are  $\text{P}\bar{3}\text{m}1$  and  $\text{P}3\text{m}1$ , respectively. Due to the inversion symmetry, both C-Metal (and also O-Metal) bonds have equal lengths in the MD-II structure. Conversely, due to absence of such inversion symmetry, we have two different bond lengths for the C-Metal and O-Metal bonds in the MD-III structure. For instance, while the C-Metal (O-Metal) bond length is  $2.19 \text{ \AA}$  ( $1.98 \text{ \AA}$ ) in MD-II of  $\text{Ti}_2\text{CO}_2$ , it becomes  $2.22$  and  $2.16 \text{ \AA}$  ( $2.00$  and  $1.98 \text{ \AA}$ ) in MD-III of  $\text{Ti}_2\text{CO}_2$ . This structural asym-

metry brings different stabilities, electronic, vibrational, thermal and thermoelectric properties in MD-III as compared to MD-II. For instance, lower stability and longer bond lengths may result in softer vibrational frequencies in the MD-III structure, thereby leading to reduced thermal conductivity.

TABLE I: Positions of valence band maximum ( $V_{max}$ ) and conduction band minimum ( $C_{min}$ ), and corresponding band gap energies for the MD-II and MD-III configurations of  $\text{M}_2\text{CO}_2$  ( $\text{M}=\text{Ti}, \text{Zr}, \text{Hf}, \text{Sc}$ ).

	MDII			MDIII		
	$E_g$ (eV)	$V_{max}$	$C_{min}$	$E_g$ (eV)	$V_{max}$	$C_{min}$
$\text{Ti}_2\text{CO}_2$	0.26	$\Gamma$	$M$	0.69	$\Gamma - K$	$\Gamma - M$
$\text{Zr}_2\text{CO}_2$	0.91	$\Gamma$	$M$	1.05	$\Gamma - K$	$\Gamma - M$
$\text{Hf}_2\text{CO}_2$	1.02	$\Gamma$	$M$	1.09	$\Gamma$	$M$
$\text{Sc}_2\text{CO}_2$	-	-	-	1.76	$\Gamma$	$K$

The calculated electronic band structures and phonon dispersion curves of all the scrutinized monolayer crystals along the high symmetry directions of the Brillouin zone are given in the Electronic Supplementary Information (ESI). The group velocity is also indicated by line color in phonon dispersion curves. Beside these, we demonstrated the total density of states and partial density of states of each atom composing  $\text{M}_2\text{CO}_2$  MXene structures in ESI (Fig. S5). As indicated in Figs. S1-S3 in ESI, MD-II and MD-III configurations of  $\text{M}_2\text{CO}_2$  ( $\text{M}=\text{Ti}, \text{Zr}, \text{Hf}$ ) were found to be indirect band semiconductors.  $\text{Sc}_2\text{CO}_2$ -MD-III has the widest indirect band gap of  $1.76 \text{ eV}$  and the MD-II configuration of  $\text{Ti}_2\text{CO}_2$  has the smallest band gap with a value of  $0.26 \text{ eV}$ . In the presence of mixed conduction due to small band gap values, the holes and electrons counteract each other, lowering power factor. In this respect, the MD-II to MD-III structural transition in  $\text{Ti}_2\text{CO}_2$  possibly suppresses the bipolar conduction at the elevated temperatures, enhancing the Seebeck coefficient. The calculated band gap values of these structures, given in Table I, are in excellent agreement with the previous calculations.<sup>22,23,30,41,43</sup> The effect of structural model on the electronic properties is the largest in  $\text{Ti}_2\text{CO}_2$  and it becomes less effective when moving from Ti to Hf. The band gap difference is  $0.40 \text{ eV}$  for  $\text{Ti}_2\text{CO}_2$ ,  $0.14 \text{ eV}$  for  $\text{Zr}_2\text{CO}_2$  and  $0.07 \text{ eV}$  for  $\text{Hf}_2\text{CO}_2$ , see Table I. Interestingly, the band gap values increase when going from Ti to Hf in both structural models. Since MD-II of  $\text{Ti}_2\text{CO}_2$  has the smallest band gap, it is expected that, at high temperatures and low carrier concentrations, both electrons and holes contribute to heat transport, and increase the overall thermal conductivity, thereby reducing the Seebeck coefficient and increasing the electrical conductivity. However, the MD-III configuration of  $\text{Ti}_2\text{CO}_2$  can exhibit enhanced TE properties due to its much larger band gap as compared to its MD-II configuration. As a representative, Figure 2 shows the band structures and orbital resolved density of states of MD-II and MD-III of  $\text{Ti}_2\text{CO}_2$ . Zr and Hf based MXenes have similar electronic properties. The valence band (VB) edge has the

main contribution coming from C-2*p* orbitals while M-*d* orbital mainly contributes to the conduction band (CB) edge in the MD-II structure. The weights of the atomic

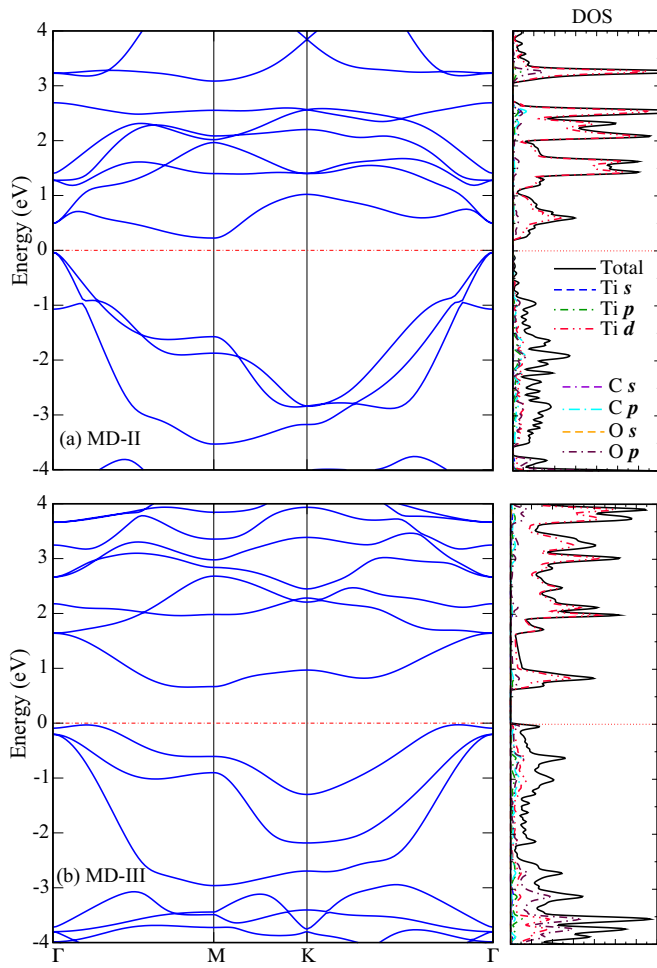


FIG. 2: (Color online) Band structure and orbital resolved density of states of (a) MD-II and (b) MD-III structures of  $\text{Ti}_2\text{CO}_2$ .

orbitals significantly change throughout the high symmetry directions in the first Brillouin zone. In MD-III, *p* orbital of oxygen atoms move towards the Fermi level and dominate the valence band edge. Concerning the valence band of the MD-III structure, there are two peaks with almost the same energies (i.e. they are all accessible by carrier doping), located at the  $\Gamma$  point and a point close to the *K* along  $\Gamma - K$  direction. It has been previously shown that such a multi-valley/peak structure in  $\text{Bi}_2\text{Te}_3$ ,  $\text{Sb}_2\text{Te}_3$ <sup>44</sup> and  $\text{SnSe}$ <sup>45</sup> leads to a large TE power factor,  $S^2\sigma$ . Therefore, in the MD-III structure, the formation of new extreme located between  $\Gamma - K$  points, which is 1 eV below in the MD-II structure, may be expected to enhance *S* and thus,  $S^2\sigma$ . Furthermore, the bands forming the lowest conduction band are very flat in both structural models, whereas the valence band of MD-II has a much larger dispersion (spreading over 3 eV). Such difference in the valence band of the MD-II and MD-III

structures give rise to a larger hole effective mass in the former, thereby leading to a significantly enhanced *p*-type Seebeck coefficient in the MD-III structure.

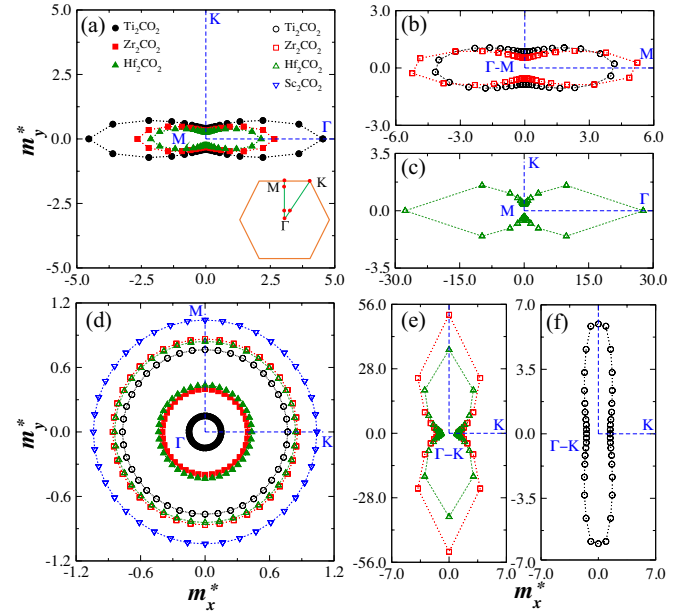


FIG. 3: (Color online) Direction dependent electron effective masses for (a) Ti, Zr, and Hf based MD-II structures, (b) Ti and Zr based MD-III structures, and (c) Hf based MD-III structure, and hole effective masses for (d) Ti, Zr, Hf, and Sc based MD-II and MD-III structures, (e) Ti and Zr based MD-III structures, and (f) Hf based MD-III structure. Here,  $\Gamma$ , *M*, *K*,  $\Gamma$ -*M*, and  $\Gamma$ -*K* depict the center of the band extrema and Brillouin zone directions. Each data point represents the end point of a vector whose amplitude corresponds to the effective mass in units of  $m_0$  and the direction of this vector corresponds to the direction (Cartesian coordinates) in the *k* space along which the mass is calculated.

The effective mass,  $m^*$ , of electrons and holes are also significantly affected from the surface termination model. The conduction band minima of all the MD-II structures and MD-III structure of  $\text{Hf}_2\text{CO}_2$  are located at the *M* point as seen in Figs. 3 (a) and (c). Whereas, the conduction band minima of  $\text{Ti}_2\text{CO}_2$  and  $\text{Zr}_2\text{CO}_2$  are close to the *M* point along the  $\Gamma - M$  direction. For all the materials, the highly anisotropic effective masses are heavier in the MD-III structure for all directions as compared to the MD-II structure. The hole effective masses at the  $\Gamma$  point are around 0.15-0.50 and 0.60-1.10  $m_0$  (where  $m_0$  is the mass of electron in free space) for MD-II and MD-III, respectively, as seen in Fig. 3 (d). However, the hole effective mass values corresponding to the newly emerged band in the MD-III structures, where the band extreme is located close to the *K* point along  $\Gamma - K$  direction, are significantly anisotropic. This band is very flat along the direction perpendicular to the  $\Gamma - K$  with hole effective masses of  $\sim 7.00$  for  $\text{Ti}_2\text{CO}_2$  and surprisingly  $>28.00 m_0$  for  $\text{Zr}_2\text{CO}_2$  and  $\text{Hf}_2\text{CO}_2$ , as seen in Figs. 3 (e) and (f).

Phonon dispersion curves for all the structures that

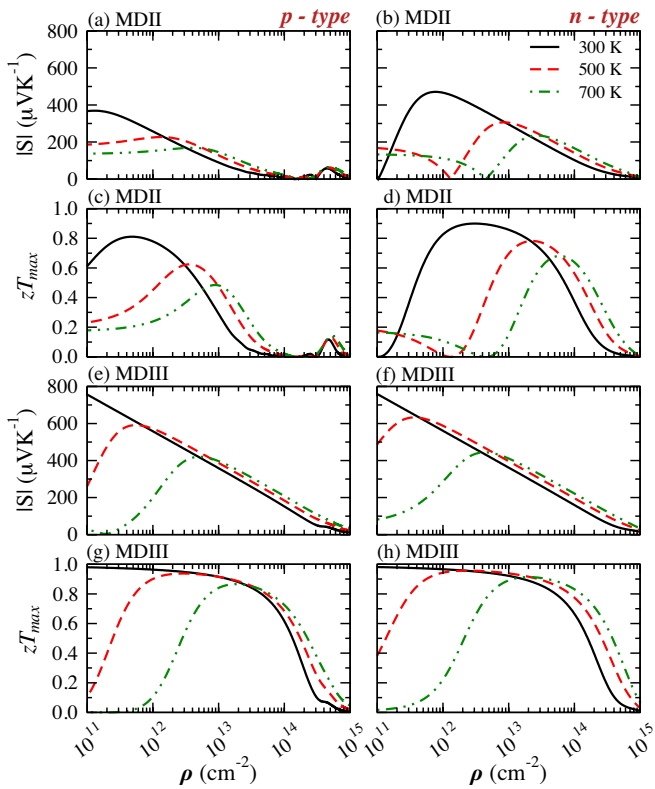


FIG. 4: (Color online) Seebeck coefficient and maximum TE figure-of-merit as a function of carrier density at  $T=300, 500, 700$  K of  $\text{Ti}_2\text{CO}_2$ . Plots for the MD-II and MD-III configurations are represented in a, b, c, d and e, f, g, h, respectively.

display positive frequencies in the whole Brillouin zone, demonstrating dynamic stability at  $T=0$  K (Figs. S6-S9 in ESI). Since there are 5 atoms in the primitive cell of  $\text{M}_2\text{CO}_2$  system, there are 15 vibrational modes: the lowest 3 of them are acoustic modes (known as in-plane longitudinal acoustic mode (LA), transverse acoustic mode (TA) and out-of-plane transverse acoustic (or flexural acoustic) mode (ZA)) and the remaining ones are optical modes. The frequencies of the in-plane LA and TA branches exhibit a linear dispersion around the  $\Gamma$  point whereas ZA branch has a quadratic dispersion in the long wavelength limit. The vibrational direction of the ZA mode is definitely perpendicular to the monolayer plane as in the other 2D structures like graphene,<sup>46</sup> phosphorene,<sup>47</sup> stanene.<sup>48</sup> The ZA mode is of great importance in understanding the thermal and mechanical properties of 2D materials.<sup>49–51</sup> The ZA branch is less dispersive in MD-III than in MD-II. In general, the group velocities of phonon modes in MD-III are usually comparable with those in MD-II when we include non-analytic term correction which mostly affects the optical modes. In all structures, there are low frequency optical branches near the acoustic branches enhancing the possibility of Umklapp scattering that involves an acoustic mode and an optical mode.<sup>52</sup> In Hf-based MXenes, the high lying optical modes are well separated from low lying ones indicating

lower probability of three-phonon scattering between the optical phonons. Hence, Hf-based MXenes have higher  $\kappa_l$ .

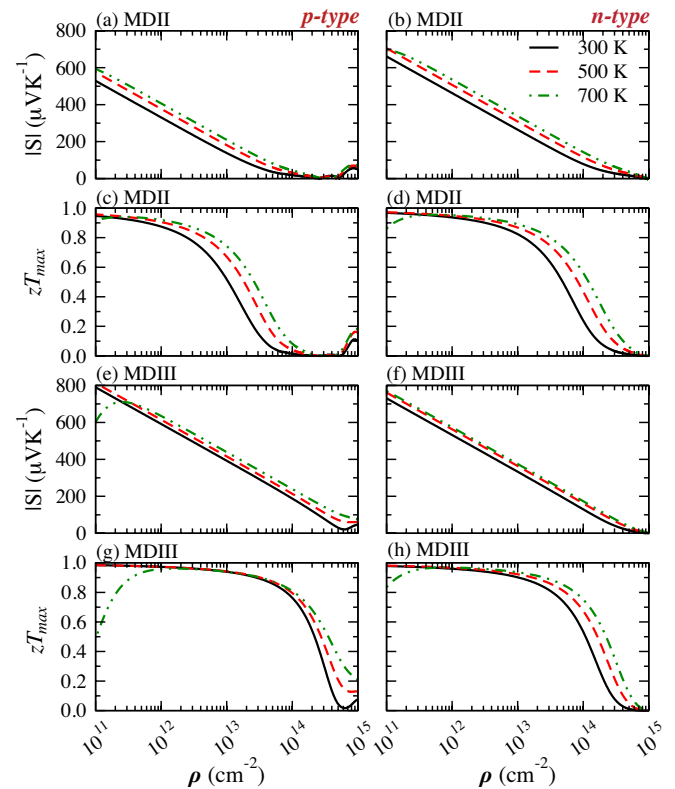


FIG. 5: (Color online) Seebeck coefficient and maximum TE figure-of-merit as a function of carrier density at  $T=300, 500, 700$  K of  $\text{Zr}_2\text{CO}_2$ . Plots for the MD-II and MD-III configurations are represented in a, b, c, d and e, f, g, h, respectively.

In order to find out TE efficiency of the considered MXene materials, we computed Seebeck coefficient, electrical conductivity and electronic thermal conductivity with constant relaxation time approximation. We first estimated the maximum value of TE figures-of-merit,  $zT_{\max}$ , with the assumption of vanishing  $\kappa_l$  ( $zT_{\max}=S^2\sigma T/\kappa_e$ ). We plotted the absolute values of Seebeck coefficients and also  $zT_{\max}$  values for both  $n$ - and  $p$ -type doping as a function of charge carrier density at three different temperatures, namely,  $T=300, 500$  and  $700$  K, in Figs. 4 to 7. The charge carrier densities were calculated by integrating the density of states for both  $p$ -type and  $n$ -type doping. At a given temperature and charge carrier density, the MD-III configurations exhibit higher Seebeck coefficients and  $zT_{\max}$  as compared to MD-II configurations. The origin of high Seebeck coefficient in the MD-III structures can be partially attributed to their more complex band structures and heavier carrier effective masses as discussed above. The influence of the configuration is more specifically observed in  $\text{Ti}_2\text{CO}_2$ , especially at lower carrier densities. Consistent with the fact that Seebeck coefficient is adversely proportional to carrier density, we have lower Seebeck coefficients at high doping concen-

trations. While the  $n$ -type Seebeck coefficient is significantly higher than  $p$ -type one in MD-II, we have comparable  $n$  and  $p$ -type Seebeck coefficients in MD-III, due to presence of the highly flat valence band in the latter. As seen from Fig. 6 (e), the  $p$ -type Seebeck coefficient of the MD-III structure of  $\text{Hf}_2\text{CO}_2$  has a different variation with carrier concentration at  $T=300$  K. The reason for this behavior can be revealed if one thoroughly inspects the band structure and density of states plots, see ESI. In contrast to the MD-III structure of  $\text{Ti}_2\text{CO}_2$  and  $\text{Zr}_2\text{CO}_2$ , which have large DOS at the top valence band due to the flat band, DOS corresponding to the top of the valence band is very small in the MD-III structure of  $\text{Hf}_2\text{CO}_2$ . This is due to fact that the flat band is slightly below the more dispersive bands in the MD-III structure of  $\text{Hf}_2\text{CO}_2$ .

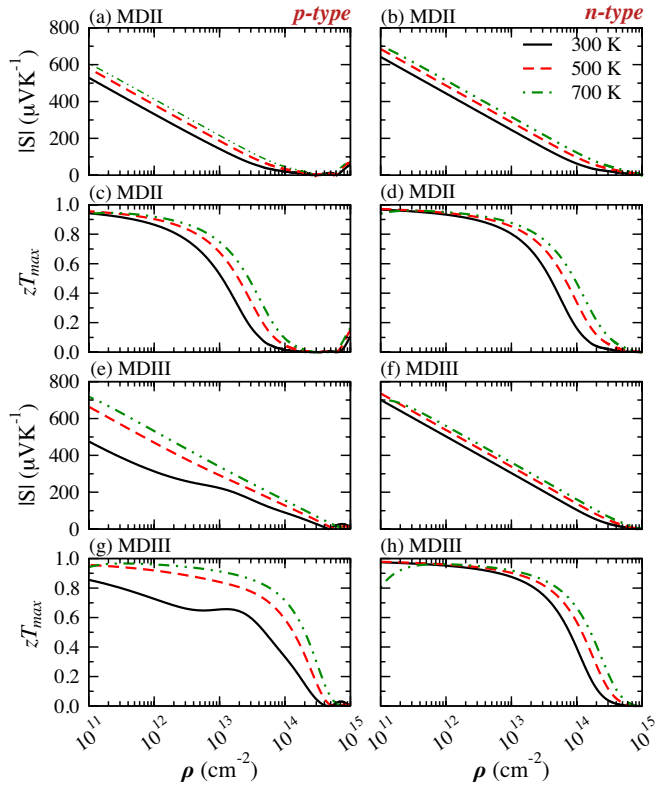


FIG. 6: (Color online) Seebeck coefficient and maximum TE figure-of-merit as a function of carrier density at  $T=300, 500, 700$  K of  $\text{Hf}_2\text{CO}_2$ . Plots for the MD-II and MD-III configurations are represented in a, b, c, d and e, f, g, h, respectively.

The maximum attainable values for the Seebeck coefficient at room temperature were found to be around 480, 680, and 650  $\mu\text{V/K}$  for the  $n$ -type carrier concentrations in MD-II configuration of  $\text{Ti}_2\text{CO}_2$ ,  $\text{Zr}_2\text{CO}_2$  and  $\text{Hf}_2\text{CO}_2$ , respectively. Both  $p$ -type and  $n$ -type carrier concentrations in the MD-III configuration of  $\text{Ti}_2\text{CO}_2$  and  $\text{Zr}_2\text{CO}_2$  acquire Seebeck coefficient of approximately 750 and 800  $\mu\text{V/K}$  (in respective order). Similarly, for  $n$ -type doping of  $\text{Hf}_2\text{CO}_2$  in the MD-III configuration the maximum Seebeck coefficient was estimated as approximately

700  $\mu\text{V/K}$ . Furthermore, the Seebeck coefficient of the  $p$ -type and  $n$ -type in the MD-III structure of  $\text{Sc}_2\text{CO}_2$  have approximate value of about 600  $\mu\text{V/K}$ . These calculated Seebeck coefficient values are comparable with, even better than, that of the well-known TE material  $\text{SrTiO}_3$ ,  $\text{Bi}_2\text{Te}_3$  nanowires, and  $\text{Te}/\text{Bi}_2\text{Te}_3$  nanowire heterostructure composites, exhibit a Seebeck coefficient of 850  $\mu\text{V/K}$  at around 90 K, 205  $\mu\text{V/K}$  at  $T=300$  K, and 608  $\mu\text{V/K}$  at  $T=300$  K, respectively.<sup>53–55</sup>

In the case of narrow band gap semiconductors, the minority carriers lead to a decrease in Seebeck coefficient with an increase in the electrical conductivity at high temperature values and low carrier densities.<sup>56</sup> As the temperature gets higher, this decrease in the Seebeck coefficient can be prominently seen in Figs. 4(c-d) and 4(g-h), because of the narrow band gap of  $\text{Ti}_2\text{CO}_2$ . This effect is rather small for Zr, Hf and Sc-based MXenes. The variation of the Seebeck coefficient as a function of carrier concentration is in well agreement with previous calculations.<sup>29</sup>

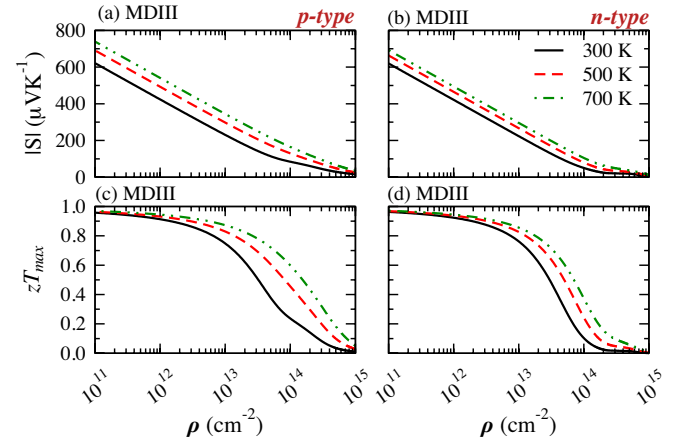


FIG. 7: (Color online) Seebeck coefficient and maximum TE figure-of-merit as a function of carrier density at  $T=300, 500, 700$  K of  $\text{Sc}_2\text{CO}_2$  for the MD-III configuration.

Based on the definition of  $zT$ , a large Seebeck coefficient together with a large ratio between electronic and lattice thermal conductivity give rise to a large  $zT$  value. As shown in Figs. 5(c-d-g-h), 6(c-d-g-h), 7(c-d), for both  $n$ -type and  $p$ -type carrier concentrations  $zT_{\text{max}}$  yields values around 0.9 – 1.0 at moderate charge carrier densities, where the  $n$ -type doped monolayers have slightly larger Seebeck coefficient and  $zT_{\text{max}}$  values as compared to the  $p$ -type doped ones. These  $zT_{\text{max}}$  results unveil that the studied MXene materials might exhibit TE performance as good as the mostly studied TE materials  $\text{Bi}_2\text{Te}_3$  and  $\text{SrTiO}_3$ , even though the maximum  $zT$  value of each one could not be larger than 1.0. At the moderate doping levels, the  $zT_{\text{max}}$  value is found to be around 0.65 and 0.7 for  $\text{Bi}_2\text{Te}_3$  and  $\text{SrTiO}_3$ , respectively.<sup>57</sup> Our calculated values are also quite promising. Essentially, oxide thermoelectric materials, including  $n$ -type  $\text{SrTiO}_3$ ,<sup>58</sup>  $\text{CaMnO}_3$ <sup>59</sup> and  $\text{ZnO}$ <sup>60</sup> and  $p$ -type

$\text{Ca}_3\text{Co}_4\text{O}_9$ <sup>61</sup> and  $\text{Na}_x\text{CoO}_2$ <sup>62</sup> have various advantages over alloy thermoelectric materials, including their resistance to high temperatures (due to their structural and chemical stability), oxidation resistance, low toxicity, easy processing, and low costs. Nevertheless, due to their very low electrical conductivity,  $zT$  values of oxides are not high enough as compared with good thermoelectric materials including  $\text{Bi}_2\text{Te}_3$ . In this respect, the semiconducting oxygen terminated MXene monolayers exhibit much better electric properties due to their electronic structure possessing lower electronic band gap values.

TABLE II: The lattice thermal conductivity,  $\kappa_l$  values for the MD-II and MD-III configurations of  $\text{M}_2\text{CO}_2$  (M=Ti, Zr, Hf, Sc) at T=300, 500 and 700 K.

$\kappa$ (W/mK)	T=300 K		T=500 K		T=700 K	
	MD-II	MD-III	MD-II	MD-III	MD-II	MD-III
$\text{Ti}_2\text{CO}_2$	40.58	18.42	22.29	10.47	15.50	7.36
$\text{Zr}_2\text{CO}_2$	50.40	16.85	28.37	9.71	19.88	6.85
$\text{Hf}_2\text{CO}_2$	57.39	27.43	31.82	15.69	22.18	11.05
$\text{Sc}_2\text{CO}_2$	(Metal)	47.01	(Metal)	25.93	(Metal)	18.06

In order to estimate the thermoelectric properties of these materials more realistically, we also investigated lattice thermal transport properties. In Figs. 8(a) and (b), we present the calculated  $\kappa_l$  values of the MD-II and MD-III configurations predicted by iterative solutions of the linearized BTE as a function of temperature, respectively. The first observation is that the MD-III structure of a particular MXene has lower  $\kappa_l$  than its MD-II structure. As is shown in Figs. S6-S9 in ESI, the ZA branch is softer in MD-III than in MD-II. Due to the reduced crystal symmetry, the ZA mode undergoes enhanced scattering, thereby suppressing the contribution of the ZA mode to the  $\kappa_l$ , see Fig. S11. Thus, the relaxation time of this mode in MD-III is quite short as compared to that in MD-II, as seen in Fig. S12. In addition, the contribution of optical phonons to the  $\kappa_l$  is quite large in these two dimensional crystals as compared to graphene<sup>63</sup> and blue phosphorus.<sup>64</sup> Figs. 8(a) and (b) show that the  $\kappa_l$  of MXenes are inversely proportional to temperature ( $T^{-1}$ ). The temperature dependence of  $\kappa_l$  of the MD-II structure of  $\text{M}_2\text{CO}_2$  (M=Ti, Zr, Hf) is in line with the values predicted by Gandhi *et al.*<sup>29</sup> We found that, in the MD-III structure, the contribution of optical phonons is significantly reduced as compared to the MD-II structure. At room temperature, all these considered materials have much lower  $\kappa_l$  as compared to monolayer graphene (2200 W/mK,<sup>46</sup> 4840 – 5300 W/mK),<sup>63</sup> hBN (360 W/mK).<sup>65</sup> Furthermore, these MXene materials have as low  $\kappa_l$  as most promising 2D materials for nano-electronic applications such as few-layer  $\text{MoS}_2$  (44-103 W/mK),<sup>66,67</sup> silicene (36.2 W/mK),<sup>68</sup> black phosphorene (110 W/mK (armchair) and 36 W/mK (zigzag)) and blue phosphorene (78 W/mK).<sup>64</sup>

For the MD-III configuration of  $\text{Ti}_2\text{CO}_2$  and  $\text{Zr}_2\text{CO}_2$ , the variation of the  $\kappa_l$  with temperature has similar behavior at all temperature values considered here. As can

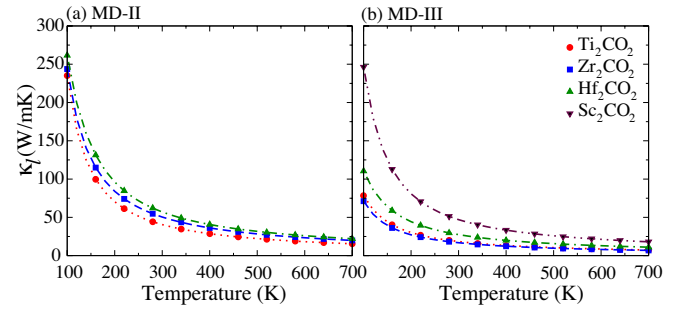


FIG. 8: (Color online) Lattice thermal conductivity,  $\kappa_l$  values as a function of temperature in the range of 100 K to 700 K for (a) the MD-II and (b) MD-III structures. The ratio of self consistent  $\kappa_l$  values ( $\kappa$ ) to RTA solutions ( $\kappa_{\text{RTA}}$ ) for (c) the MD-II and (d) MD-III structures.

be seen from Fig. 8(b), the  $\kappa_l$  of  $\text{Sc}_2\text{CO}_2$ -MD-III is noticeably higher than the values corresponding to the others for the temperature values below 300 K. The calculated  $\kappa_l$  values at T=300 K, 500 K and 700 K are given in Table II. The MD-III configuration of  $\text{Ti}_2\text{CO}_2$  and  $\text{Zr}_2\text{CO}_2$  have the lowest  $\kappa_l$  as compared to the others in both MD-II and MD-III configurations. Among all the considered structures,  $\text{Hf}_2\text{CO}_2$  in the MD-II configuration has the highest  $\kappa_l$ . This higher value partially is a result of the large gap between acoustic and optical phonon branches in its phonon dispersion curve (Fig. S8 in ESI) that reduces the three-phonon scattering processes.<sup>69,70</sup> The calculated  $\kappa_l$  of  $\text{Sc}_2\text{CO}_2$  in MD-III is 47 W/mK at T=300 K, consistent with the value of 59 W/mK reported in a previous study.<sup>71</sup> For the MD-II configuration, the  $\kappa_l$  increases as the atomic number of M (M=Ti, Zr, Hf) increases whereas the MD-III configurations exhibit abnormal trend, most likely due to the distinct nature of Umklapp scattering processes. Similar result was also predicted for monolayer  $\text{MoS}_2$  and  $\text{WS}_2$  crystals.<sup>67</sup>

Subsequent to the first principles  $\kappa_l$  calculations, we determined the  $zT = S^2\sigma T/(\kappa_e + \kappa_l)$  within constant electronic relaxation time approximation for both  $p$ - and  $n$ -type doping. Figure 9 shows the carrier density dependency of the calculated  $zT$  values for each monolayer MXene crystal. Here, the relaxation time of holes and electrons were fixed to 10 fs ( $\tau = 10^{-14}$  s) as proposed by Ref. 25. Because of the fact that the Seebeck coefficient has higher values and also the  $\kappa_l$  has lower values in the MD-III configuration, the  $zT$  of the MD-III configurations tends to get larger values compared to the MD-II structures. Similar to our assumption of vanishing  $\kappa_l$ , this approximation also puts an upper bound for  $zT$  values.  $zT$  gets its maximum attainable value for the charge densities around  $10^{13}$ - $10^{14}$   $\text{cm}^{-2}$  for all the considered systems. Our results clearly showed the notable influence of the functionalization on the electronic, thermal, and thermoelectric properties, consistent with the previous findings, which demonstrated the strong influence of functionalization on the electronic properties.<sup>72</sup> The plots of temperature dependent maximum  $zT$  values,



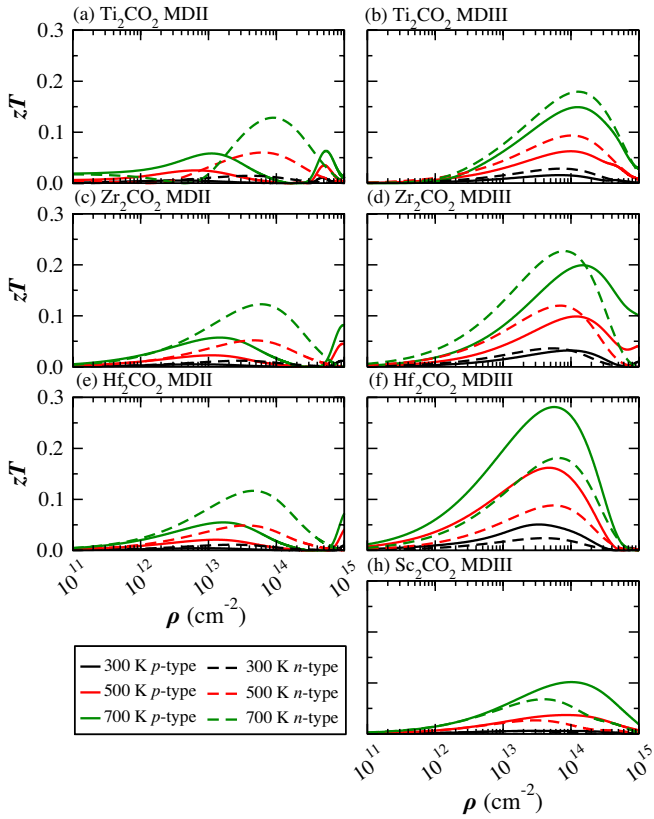


FIG. 9: (Color online)  $zT$  as a function of carrier density using constant relaxation time approximation with  $\tau = 10$  fs for  $p$ -type and  $n$ -type doping.

calculated for  $\tau = 5$  fs and 15 fs, are shown in Figures 10 (a) and (b). As expected, the longer relaxation times give rise to larger  $zT_{max}$  values. Figure 10 also demonstrates the importance of surface functionalization discussed above. For instance, while  $n$ -type doping yields larger  $zT_{max}$  values for all MD-II structures, either  $n$ -type or  $p$ -type doping may yield to larger  $zT_{max}$  values depending on the metal type for MD-III structures. In this work, we did not consider the random functionalization of O atoms due to the significant computational cost, in particular in thermal conductivity calculations. However, it is a clear fact that the thermal conductivity can be controlled by random arrangement, which can affect the thermoelectric properties of the studied materials positively.

Thermoelectric materials require the contradictory properties of high electron mobility, large Seebeck coefficient and low thermal conductivity. High thermoelectric efficiencies can be realized by exploiting different approaches including improving carrier mobility and concentration by doping, enhancing Seebeck coefficient by band structure engineering, and reducing thermal conductivity by nanostructuring and introducing structural imperfections.<sup>73,74</sup> In this work, we found that lowering the crystal symmetry of MXene monolayers can double  $zT$  values. Similar to the intrinsic defects, the dopant

elements create structural imperfections in the lattice of MXene crystals, which are expected to limit the phonon mean free paths significantly and results in a suppressed phonon transport. Since the dominant heat carriers in semiconductors and insulators are phonons, a reduced thermal conductivity and an improved thermoelectric performance can be achieved. In addition, by exploiting doping, we can also enhance electrical conductivity by optimizing carrier concentrations to increase power factor (i.e.  $S^2\sigma$ ). As we have already shown that the acoustic phonon modes with large wave lengths (small wave numbers) dominate the thermal transport in both MD-II and MD-III structures due to their large group velocities, see SM. Therefore, MXene flakes with in-plane dimensions comparable or smaller than mean free paths of main heat carriers lead to enhanced phonon scattering at interfaces and can attain low thermal conductivity values. We can also avoid the excitation of such phonons by adjusting the size of the MXene flakes. Combining this strategy (i.e. nanostructuring proposed by Dresselhaus and coworkers)<sup>75</sup> with band structure engineering to optimize the power factor by altering the electronic structure appears as a promising way to enhanced thermoelectric efficiency.

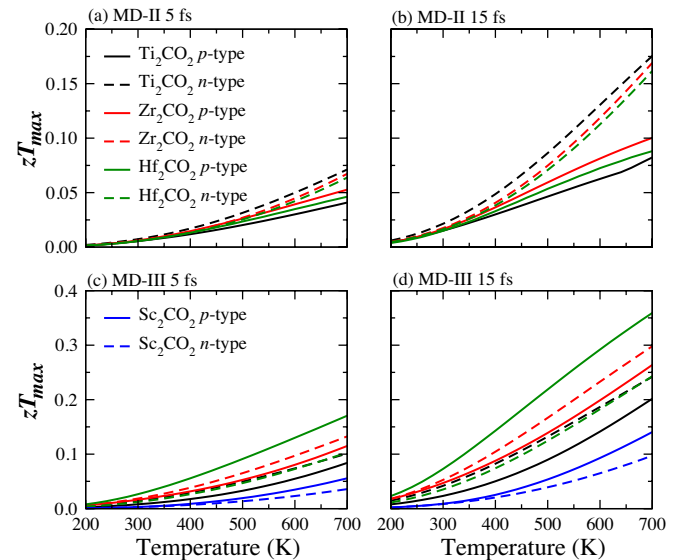


FIG. 10: (Color online)  $zT_{max}$  as a function of temperature using constant relaxation time approximation with  $\tau = 5$  fs and  $\tau = 15$  fs.

Finally, we discussed the effect of long range electrostatic interactions on the thermal properties. We note that, due to finite band gap and presence of mixed ionic-covalent bonds, these structures have appreciable Born effective charges. Our calculation showed that such long range electrostatic interactions give rise to a splitting of LO and TO branches. However, this splitting slightly modifies the thermal properties. This is correlated with the fact that the optical branches have very small contribution to  $\kappa_l$  as compared to acoustic branches. Despite

this, it's very likely to be an erroneous assumption to neglect the optical modes due to the fact that the optical modes are crucial to provide channels for acoustic phonon scattering.

#### IV. CONCLUSION

We investigated the thermal transport properties (Seebeck coefficient,  $\kappa_l$ , TE figure-of-merit) of oxygen-functionalized  $M_2CO_2$  (where  $M=Ti, Zr, Hf, Sc$ ) MXenes with two different configurations by using phonon Boltzmann transport theory combined with first-principles calculations. Our results revealed that the MD-III configurations of  $M_2CO_2$  ( $M=Ti, Zr, Hf, Sc$ ) structures with larger band gaps exhibit larger Seebeck coefficients than  $M_2CO_2$  structures in MD-II configuration. The MD-II and MD-III configurations of  $Zr_2CO_2$  and  $Hf_2CO_2$  exhibit nearly the same TE properties whereas the same configurations of  $Ti_2CO_2$  have very distinct TE properties. The effect of structural model on the TE properties is the largest in  $Ti_2CO_2$ .  $Ti_2CO_2$  in the MD-II structure possess weaker TE efficiency than other structures because of having lowest Seebeck coefficient values. At room temperature, monolayer  $Sc_2CO_2$  with MD-III configuration has the maximum Seebeck coefficient. The TE performance of the MD-II structures is generally weak at room temperature, because of having relatively larger  $\kappa_l$  and smaller Seebeck coefficient. The calculated  $\kappa_l$  values are much lower than that of graphene whereas they are

comparable to that of  $MoS_2$ , silicene and phosphorane. We also found that the largest contribution to  $\kappa_l$  is given by acoustic phonons. Due to enhanced scattering of ZA mode as a result of reduced crystal symmetry, the MD-III structures have lower  $\kappa_l$  as compared to the MD-II ones. The contribution of each phonon mode to  $\kappa_l$ , relaxation time and MFP provide great guidance to experimental efforts and also shed light on nanodesigning of MXene based TE materials. The structural variety provides us an additional degree of freedom for modulating physical and chemical properties of MXenes, that can be exploited to design efficient thermoelectric devices.

#### Acknowledgments

We acknowledge the support from Scientific and Technological Research Council of Turkey (TUBITAK-116F080). A part of this work was supported by the BAGEP Award of the Science Academy. Computational resources were provided by TUBITAK ULAKBIM, High Performance and Grid Computing Center (TRGrid e-Infrastructure) and Istanbul Technical University, National Center for High Performance Computing (UHeM). This work was performed, in part, at the Center for Nanoscale Materials, a U.S. Department of Energy Office of Science User Facility, and supported by the U.S. Department of Energy, Office of Science, under Contract No. DE-AC02-06CH11357.

\* Electronic address: sevil.sarikurt@deu.edu.tr

† deniz.cakir@und.edu

‡ keceli@anl.gov

§ csevik@anadoluldu.edu.tr

<sup>1</sup> K. S. Novoselov, A. K. Geim, S. V. Morozov, D. Jiang, Y. Zhang, S. V. Dubonos, I. V. Grigorieva and A. A. Firsov, *Science*, 2004, **306(5696)**, 666–669.

<sup>2</sup> M. Naguib, O. Mashtalir, J. Carle, V. Presser, J. Lu, L. Hultman, Y. Gogotsi and M. W. Barsoum, *ACS Nano*, 2012, **6(2)**, 1322–1331.

<sup>3</sup> M. Naguib, M. Kurtoglu, V. Presser, J. Lu, J. Niu, M. Heon, L. Hultman, Y. Gogotsi and M. W. Barsoum, *Advanced Materials*, 2011, **23(37)**, 4248–4253.

<sup>4</sup> M. Naguib, J. Halim, J. Lu, K. M. Cook, L. Hultman, Y. Gogotsi and M. W. Barsoum, *Journal of the American Chemical Society*, 2013, **135(43)**, 15966–15969.

<sup>5</sup> M. Ghidui, M. Naguib, C. Shi, O. Mashtalir, L. M. Pan, B. Zhang, J. Yang, Y. Gogotsi, S. J. L. Billinge and M. W. Barsoum, *Chemical Communications*, 2014, **50(67)**, 9517–9520.

<sup>6</sup> R. Meshkian, L.-A. Naslund, J. Halim, J. Lu, M. W. Barsoum and J. Rosen, *Scripta Materialia*, 2015, **108**, 147–150.

<sup>7</sup> B. Anasori, Y. Xie, M. Beidaghi, J. Lu, B. C. Hosler, L. Hultman, P. R. C. Kent, Y. Gogotsi and M. W. Barsoum, *ACS Nano*, 2015, **9(10)**, 9507–9516.

<sup>8</sup> P. Urbankowski, B. Anasori, T. Makaryan, D. Er, S. Kota, P. L. Walsh, M. Zhao, V. B. Shenoy, M. W. Barsoum and Y. Gogotsi, *Nanoscale*, 2016, **8(22)**, 11385–11391.

<sup>9</sup> M. Naguib, J. Come, B. Dyatkin, V. Presser, P.-L. Taberna, P. Simon, M. Barsoum and Y. Gogotsi, *Electrochemistry Communications*, 2012, **16(1)**, 61–64.

<sup>10</sup> H. Liu, D. Su, R. Zhou, B. Sun, G. Wang and S. Z. Qiao, *Advanced Energy Materials*, 2012, **2(8)**, 970–975.

<sup>11</sup> Q. Tang, Z. Zhou and P. Shen, *Journal of the American Chemical Society*, 2012, **134(40)**, 16909–16916.

<sup>12</sup> D. Er, J. Li, M. Naguib, Y. Gogotsi and V. B. Shenoy, *ACS Applied Materials & Interfaces*, 2014, **6(14)**, 11173–11179.

<sup>13</sup> M. R. Lukatskaya, O. Mashtalir, C. E. Ren, Y. Dall'Agnesse, P. Rozier, P. L. Taberna, M. Naguib, P. Simon, M. W. Barsoum and Y. Gogotsi, *Science*, 2013, **341(6153)**, 1502–1505.

<sup>14</sup> M. Ghidui, M. R. Lukatskaya, M.-Q. Zhao, Y. Gogotsi and M. W. Barsoum, *Nature*, 2014, **516(7529)**, 78–81.

<sup>15</sup> H. Tang, J. Wang, H. Yin, H. Zhao, D. Wang and Z. Tang, *Advanced Materials*, 2015, **27(6)**, 1117–1123.

<sup>16</sup> M. Naguib, V. Mochalin, M. Barsoum and Y. Gogotsi, *Advanced Materials*, 2014, **26(7)**, 992–1005.

<sup>17</sup> Q. Hu, D. Sun, Q. Wu, H. Wang, L. Wang, B. Liu, A. Zhou and J. He, *The Journal of Physical Chemistry A*, 2013, **117(51)**, 14253–14260.

<sup>18</sup> Q. Hu, H. Wang, Q. Wu, X. Ye, A. Zhou, D. Sun, L. Wang,

- B. Liu and J. He, *International Journal of Hydrogen Energy*, 2014, **39**(20), 10606–10612.
- <sup>19</sup> L.-Y. Gan, Y.-J. Zhao, D. Huang and U. Schwingenschlgl, *Physical Review B*, 2013, **87**(24), 245307.
- <sup>20</sup> Z. Ma, Z. Hu, X. Zhao, Q. Tang, D. Wu, Z. Zhou and L. Zhang, *The Journal of Physical Chemistry C*, 2014, **118**(10), 5593–5599.
- <sup>21</sup> H. Kim, B. Anasori, Y. Gogotsi and H. N. Alshareef, *Chemistry of Materials*, 2017, **29**, 6472–6479.
- <sup>22</sup> M. Khazaei, M. Arai, T. Sasaki, C. Y. Chung, N. S. Venkataramanan, M. Estili, Y. Sakka and Y. Kawazoe, *Advanced Functional Materials*, 2013, **23**(17), 2185–2192.
- <sup>23</sup> X.-H. Zha, K. Luo, Q. Li, Q. Huang, J. He, X. Wen and S. Du, *EPL (Europhysics Letters)*, 2015, **111**(2), 26007.
- <sup>24</sup> Q. Peng, J. Guo, Q. Zhang, J. Xiang, B. Liu, A. Zhou, R. Liu and Y. Tian, *Journal of the American Chemical Society*, 2014, **136**(11), 4113–4116.
- <sup>25</sup> M. Khazaei, M. Arai, T. Sasaki, M. Estili and Y. Sakka, *Physical Chemistry Chemical Physics*, 2014, **16**(17), 7841–7849.
- <sup>26</sup> Y. Xie, M. Naguib, V. N. Mochalin, M. W. Barsoum, Y. Gogotsi, X. Yu, K.-W. Nam, X.-Q. Yang, A. I. Kolesnikov and P. R. C. Kent, *Journal of the American Chemical Society*, 2014, **136**(17), 6385–6394.
- <sup>27</sup> X.-H. Zha, J. Zhou, Y. Zhou, Q. Huang, J. He, J. S. Francisco, K. Luo and S. Du, *Nanoscale*, 2016, **8**(11), 6110–6117.
- <sup>28</sup> X.-H. Zha, Q. Huang, J. He, H. He, J. Zhai, J. S. Francisco and S. Dua, *Scientific Reports*, 2016, **6**, 27971.
- <sup>29</sup> A. N. Gandi, H. N. Alshareef and U. Schwingenschl"ogl, *Chemistry of Materials*, 2016, **28**(6), 1647–1652.
- <sup>30</sup> U. Yorulmaz, A. 'Ozden, N. K. Perkg'oz, F. Ay and C. Sevik, *Nanotechnology*, 2016, **27**(33), 335702.
- <sup>31</sup> M. Omini and A. Sparavigna, *Physica B: Condensed Matter*, 1995, **212**, 101–112.
- <sup>32</sup> D. Nika, E. Pokatilov, A. Askerov and A. Balandin, *Physical Review B*, 2009, **79**, 155413.
- <sup>33</sup> D. Nika, S. Ghosh, E. Pokatilov and A. Balandin, *Applied Physics Letters*, 2009, **94**, 203103.
- <sup>34</sup> G. Kresse and J. Hafner, *Physical Review B*, 1993, **47**(1), 558.
- <sup>35</sup> G. Kresse and J. Hafner, *Physical Review B*, 1994, **49**(20), 14251.
- <sup>36</sup> J. P. Perdew, K. Burke and M. Ernzerhof, *Physical Review Letters*, 1996, **77**, 3865.
- <sup>37</sup> H. J. Monkhorst and J. D. Pack, *Phys. Rev. B*, 1976, **13**, 5188–5192.
- <sup>38</sup> J. Ziman, *Electrons and Phonons: The Theory of Transport Phenomena in Solids*, Oxford University Press, 1960.
- <sup>39</sup> W. Li, J. Carrete, N. A. Katcho and N. Mingo, *Computer Physics Communications*, 2014, **185**(6), 1747–1758.
- <sup>40</sup> A. Togo and I. Tanaka, *Scripta Materialia*, 2015, **108**, 1–5.
- <sup>41</sup> L.-Y. Gan, D. Huang and U. Schwingenschlgl, *J. Mater. Chem. A*, 2013, **1**, 13672–13678.
- <sup>42</sup> G. K. Madsen and D. J. Singh, *Computer Physics Communications*, 2006, **175**(1), 67–71.
- <sup>43</sup> Y. Xie and P. Kent, *Physical Review B*, 2013, **87**, 235441.
- <sup>44</sup> G. Wang and T. Cagin, *Phys. Rev. B*, 2007, **76**, 075201.
- <sup>45</sup> L.-D. Zhao, G. Tan, S. Hao, J. He, Y. Pei, H. Chi, H. Wang, S. Gong, H. Xu, V. P. Dravid, C. Uher, G. J. Snyder, C. Wolverton and M. G. Kanatzidis, *Science*, 2016, **351**, 141–144.
- <sup>46</sup> B. D. Kong, S. Paul, M. B. Nardelli and K. W. Kim, *Physical Review B*, 2009, **80**, 033406.
- <sup>47</sup> G. Qin, Q.-B. Yan, Z. Qin, S.-Y. Yue, M. Hu and G. Su, *Physical Chemistry Chemical Physics*, 2015, **17**, 4854–4858.
- <sup>48</sup> B. Peng, H. Zhang, H. Shao, Y. Xu, X. Zhang and H. Zhu, *Scientific Reports*, 2016, **6**, 20225.
- <sup>49</sup> N. Bonini, J. Garg and N. Marzari, *Nano Letters*, 2012, **12**, 2673–2678.
- <sup>50</sup> G. Fugallo, A. Cepellotti, L. Paulatto, M. Lazzeri, N. Marzari and F. Mauri, *Nano Letters*, 2014, **14**, 6109–6114.
- <sup>51</sup> J. Carrete, W. Li, L. Lindsay, D. A. Broido, L. J. Gallego and N. Mingo, *Materials Research Letters*, 2016, **4**, 204–211.
- <sup>52</sup> S. Ghosh, W. Bao, D. L. Nika, S. Subrina, E. P. Pokatilov, C. N. Lau and A. A. Balandin, *Nature Materials*, 2010, **9**, 555–558.
- <sup>53</sup> H. Ohta, S. Kim, Y. Mune, T. Mizoguchi, K. Nomura, S. Ohta, T. Nomura, Y. Nakanishi, Y. Ikuhara, M. Hirano *et al.*, *Nature materials*, 2007, **6**, 129–134.
- <sup>54</sup> G. Zhang, B. Kirk, L. A. Jauregui, H. Yang, X. Xu, Y. P. Chen and Y. Wu, *Nano letters*, 2011, **12**, 56–60.
- <sup>55</sup> G. Zhang, H. Fang, H. Yang, L. A. Jauregui, Y. P. Chen and Y. Wu, *Nano letters*, 2012, **12**, 3627–3633.
- <sup>56</sup> A. F. May, M. A. McGuire, D. J. Singh, J. Ma, O. Delaire, A. Huq, W. Cai and H. Wang, *Phys. Rev. B*, 2012, **85**, 035202.
- <sup>57</sup> C. Sevik and T. Çağın, *Physical Review B*, 2010, **82**, 045202.
- <sup>58</sup> S. Ohta, T. Nomura, H. Ohta and K. Koumoto, *Journal of applied physics*, 2005, **97**, 034106.
- <sup>59</sup> D. Flahaut, T. Mihara, R. Funahashi, N. Nabeshima, K. Lee, H. Ohta and K. Koumoto, *Journal of Applied Physics*, 2006, **100**, 084911.
- <sup>60</sup> Y. Yin, B. Tudu and A. Tiwari, *Vacuum*, 2017, **146**, 356–374.
- <sup>61</sup> R. Funahashi, I. Matsubara, H. Ikuta, T. Takeuchi, U. Mizutani and S. Sodeoka, *Japanese Journal of Applied Physics*, 2000, **39**, L1127.
- <sup>62</sup> I. Terasaki, Y. Sasago and K. Uchinokura, *Physical Review B*, 1997, **56**, R12685.
- <sup>63</sup> A. A. Balandin, S. Ghosh, W. Bao, I. Calizo, D. Teweldebrhan, F. Miao and C. N. Lau, *Nano Letters*, 2008, **8**, 902–907.
- <sup>64</sup> A. Jain and A. J. McGaughey, *Scientific Reports*, 2015, **5**, 8501.
- <sup>65</sup> I. Jo, M. T. Pettes, J. Kim, K. Watanabe, T. Taniguchi, Z. Yao and L. Shi, *Nano Letters*, 2013, **13**, 550–554.
- <sup>66</sup> I. Jo, M. T. Pettes, E. Ou, W. Wu and L. Shi, *Applied Physics Letters*, 2014, **104**, 201902.
- <sup>67</sup> B. Peng, H. Zhang, H. Shao, Y. Xu, X. Zhang and H. Zhu, *RSC Adv.*, 2016, **6**, 5767–5773.
- <sup>68</sup> H. Xie, T. Ouyang, E. Germaneau, G. Qin, M. Hu and H. Bao, *Phys. Rev. B*, 2016, **93**, 075404.
- <sup>69</sup> A. Jain and A. J. McGaughey, *Journal of Applied Physics*, 2014, **116**, 073503.
- <sup>70</sup> T. Feng and X. Ruan, *Journal of Nanomaterials*, 2014, **2014**, 1–25.
- <sup>71</sup> S. Kumar and U. Schwingenschl"ogl, *Phys. Rev. B*, 2016, **94**, 035405.
- <sup>72</sup> B. Anasori, M. R. Lukatskaya and Y. Gogotsi, *Nature Reviews Materials*, 2017, **2**, 16098.
- <sup>73</sup> C.-C. Lin, R. Lydia, J. H. Yun, H. S. Lee and J. S. Rhyee, *Chemistry of Materials*, 2017, **29**, 5344–5352.

<sup>74</sup> T. Zhu, Y. Liu, C. Fu, J. P. Heremans, J. G. Snyder and X. Zhao, *Advanced Materials*, 2017, **29**, 1605884–n/a.

<sup>75</sup> M. S. Dresselhaus, G. Chen, M. Y. Tang, R. G. Yang,

H. Lee, D. Z. Wang, Z. F. Ren, J.-P. Fleurial and P. Gogna, *Advanced Materials*, 2007, **19**, 1043–1053.